Fast imaging of edge localized mode structure and dynamics in DIII-D

J. H. Yu,[1] J. A. Boedo,[1] E. M. Hollmann,[1] R. A. Moyer,[1] D. L. Rudakov,[1] and P. B. Snyder[2]
[1]*University of California at San Diego, La Jolla, California 92093, USA*
[2]*General Atomics, San Diego, California 92186, USA*

(Received 7 December 2007; accepted 25 February 2008; published online 28 March 2008)

Fast-framing images of CIII and D_α emission in the low-field-side plasma boundary of the DIII-D tokamak [J. L. Luxon, Nucl. Fusion **42**, 614 (2002)] show that edge localized modes (ELMs) rapidly eject multiple field-aligned filaments from the plasma edge. The toroidal and poloidal mode numbers of these filaments depend on normalized plasma density, with measured ELM toroidal mode numbers ranging from $\leqslant 10$ to 20 in low-density plasmas and 15 to 35 in high-density plasmas. In high-density plasmas with moderate collisionality $\nu^*_{\mathrm{ped}}=0.50$, ELMs originate at the low-field-side midplane region and the ion parallel velocity in the scrape-off layer is faster for ELMs with larger D_α divertor emission, suggesting that large ELMs eject higher-temperature ions from deeper within the plasma compared to small ELMs. In low-density plasmas with collisionality $\nu^*_{\mathrm{ped}}=0.25$, the midplane and divertor ELM signals appear simultaneously, indicating that ELM behavior depends on collisionality. At all ν^*_{ped}, ELMs drive parallel fluxes to the divertor; in addition, ELMs drive cross-field propagation of filaments, which results in plasma-wall interactions that are poloidally localized within 15 cm of the midplane. Using the wall interactions as signatures of the filaments in the scrape-off layer, the measured poloidal width of the filament ranges from 1 to 5 cm. © *2008 American Institute of Physics*. [DOI: 10.1063/1.2898404]

I. INTRODUCTION

Edge localized modes (ELMs)[1–3] are an important area of research because of their potentially damaging effects on plasma facing components in ITER and because ELMs limit the pressure pedestal height, which in turn affects overall fusion performance in a tokamak. ELMs are repetitive events observed during enhanced tokamak confinement regimes (H-mode)[4] that result in the rapid loss of particles and heat from the plasma edge. Plasma ejected into the scrape-off layer (SOL) is transported along field lines to the divertor and also across field lines resulting in plasma-surface interactions at the outer wall for sufficiently large radial particle fluxes. A typical ELM occurs on a fast time scale (200 μs–1 ms), and the transient peak power deposited by ELMs may exceed the material limits in future tokamaks. According to current modeling and experimental observations, a carbon or tungsten divertor in ITER will be able to tolerate an acceptable number of ELMs ($>10^6$) if the ELM-induced pedestal energy loss $\Delta W_{\mathrm{ELM}}/W_{\mathrm{PED}}$ is 15% or less,[5] where the pedestal energy W_{PED} is defined as $3/2$ the pedestal pressure times the plasma volume. Existing observations of $\Delta W_{\mathrm{ELM}}/W_{\mathrm{PED}}$ range from $<5\%$ to 40%, with a higher pedestal energy loss at lower collisionality.[6] Therefore, complete physics understanding of the instabilities that drive ELMs, the filament radial propagation and parallel transport of particles, and the ELM deposition and erosion processes are needed to accurately predict the impact of ELMs in future tokamaks. In addition, ELM-like bursts are observed in stellarators,[7–9] which may provide additional clues to the underlying physics of ELMs.

ELMs have been studied extensively in DIII-D,[10–13] Mega Ampere Spherical Tokamak (MAST),[14,15] Axially Symmetric Divertor Experiment (ASDEX) Upgrade,[16,17] Alcator C-Mod,[18,19] Joint European Torus (JET),[20,21] National Spherical Torus Experiment (NSTX),[22,23] Japan Atomic Energy Research Institute Tokamak-60 Upgrade (JT-60U),[24,25] and elsewhere using Langmuir probes, photodiodes, magnetic probes, and optical imaging. The broad spatial coverage provided by imaging[26–29] has proven extremely useful in understanding the global structure of ELMs, and fast imaging allows dynamics to be studied in detail. Here we expand on previous measurements and present fast-framed midplane images of ELMs in the low-field plasma edge of the DIII-D tokamak. We find that ELMs are helical filamentary structures that rotate and rapidly expand radially during the nonlinear phase known as the ELM crash. The inferred toroidal mode number n ranges from $\leqslant 10$ to 35, and the mode number depends on plasma density.[30] The poloidal width of the filament ranges from 1 to 5 cm, and cross-field transport results in ELM-wall interactions[31] that are localized to within ± 15 cm of the midplane. The measured time delay of the ELM signal between the midplane and divertor shows a qualitative difference in ELM behavior in low- and high-density regimes, and the data suggest ELMs may be caused by a current-driven peeling instability at low density and a coupled peeling-ballooning instability at high density.

II. EXPERIMENTAL SETUP

The experiments presented here utilize a lower single-null plasma configuration with plasma current $I_p=1.0-1.6$ MA and toroidal field $B_T=2$ T at the magnetic axis with major radius $R=1.8$ m and mean minor radius $\langle a\rangle=0.6$ m. Injected neutral beam power is $P_{\mathrm{NBI}}=5-9$ MW.

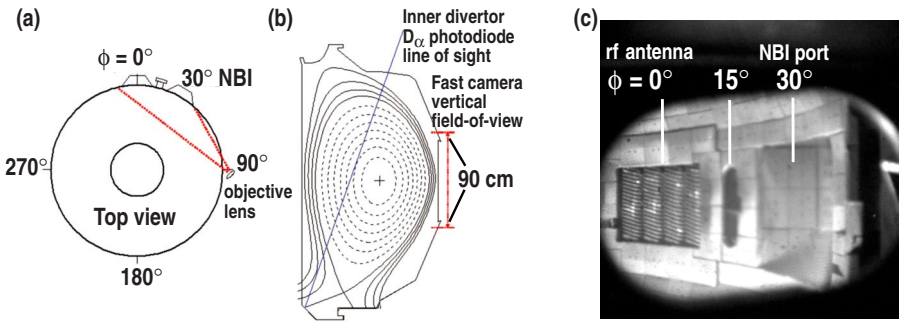

FIG. 1. (Color online) Top view (a) and side view (b) of the tokamak show the fast camera viewing angle and vertical field-of-view, which covers approximately 90 cm. (c) The camera view inside DIII-D. The plasma shape in (b) corresponds to the high plasma density cases presented in the paper.

The fast camera is located approximately 2 m from the vessel due to space limitations and neutron shielding requirements. Figure 1(a) shows the semitangential view of the plasma emission viewed through a midplane window at toroidal angle ϕ=90 deg. An objective lens focuses the light onto the front face of an 8×10 mm coherent fiber-optic bundle. Over time, fusion neutrons degrade the transmission of the fiber bundle, particularly in the blue range of the visible spectrum, requiring that the bundle be periodically replaced. Light coming out the back of the fiber bundle is collimated and passed through an optical filter, and focused onto a Vision Research Phantom v7.1 camera CMOS detector. The spatial resolution of the detector is typically 256×256 with 1 pixel imaging 0.1–0.5 cm^2, depending on the location within the field of view. At this resolution, the camera is capable of storing 21685 frames from one continuous movie with a maximum frame rate of 26000 frames/s. Typical bandpass filters used here include central wavelengths of 465 nm for CIII emission and 656 nm for D_α emission. Figure 1(b) shows the line of sight for separate photodiode measurements of D_α light from the inner divertor. These measurements are compared to the outer-midplane fast camera measurements and are used to calculate the parallel propagation time of ELMs in the SOL. The unfiltered camera view inside the DIII-D vessel is shown in Fig. 1(c), with the rf antenna at ϕ=0 and the neutral beam injection (NBI) port at ϕ=30 deg.

III. ELM IMAGES

Figure 2(a) shows images of an ELM-driven plasma in CIII light at four successive times marked in Fig. 2(b). Light from CIII emission is due to excitation of inherent carbon in the SOL from the carbon wall tiles,[32] and the tangential view of CIII emission provides direct visualization of the plasma edge. The low signal level in CIII light limits the frame rate to $\leqslant$5000 frames/s, and here the exposure time is 180 μs with electron pedestal density $n_{e,\mathrm{ped}}=5.5\times10^{13}$ cm^{-3}.

The first image of Fig. 2(a) shows that ELMs begin with a poloidally and toroidally localized unstable filament or group of filaments that bulges radially outward near the low-field-side midplane. The first image was created by subtracting a 150-frame average background inter-ELM image, showing only the perturbation with a maximum color scale equal to 1/5 that of the other three images. A dominant filament can be seen in the foreground of the first image, with an apparent pitch angle opposite that of the filaments seen in the background (near the wall in the other images) because this foreground filament is located immediately in front of the viewport at ϕ=90 deg. The observed filament pitch angle is roughly consistent with the magnetic field pitch angle expected from edge EFIT[33] equilibrium reconstruction values. During the nonlinear phase of the ELM (images 2 and 3), filaments convectively move radially outward at a mean velocity $\langle v_r\rangle\sim500\pm400$ m/s (measured from camera imaging) through the SOL after ejection from the plasma edge. The radial displacement of the tangential emission region is seen by comparing the vertical dashed line in the first and third images. The integrated emission increases by a factor of 2 to 4 as particles are ejected outward and excite CIII ions that exist in the SOL region, which corresponds to a temperature range of $T_e\sim6-10$ eV in DIII-D.[34]

Figure 2(b) shows the ELM time signal obtained by integrating the CIII emission intensity from all pixels within each camera frame, and the D_α signal (dashed) measured at the inner divertor is shown for reference. Comparing these signals (Sec. V) indicates that the ELM originates at the outer-midplane, in agreement with previous fast bolometer analysis,[35] and supporting the theoretical picture of ELMs driven by the peeling-ballooning instability.[36,37] However, in lower collisionality plasmas, the peak midplane and divertor ELM signals appear simultaneously, possibly indicating a more poloidally symmetric mode structure for the large ELMs seen in low-density plasmas.

Sequential images in D_α light during a typical ELM-wall interaction are shown in Fig. 3(a), with exposure time of 31 μs. In the inter-ELM quiet phase shown in the first image, the tangential emission region is faintly visible at the right side of the image. The D_α emission region is located $\sim1-2$ cm deeper into the plasma radially compared to the CIII emission region, because fast charge-exchange D neutrals penetrate deeper into the pedestal (before they get excited) compared to CIII ions. In the second image, a filament hits the wall and the bright stripe of emission is caused by release of neutrals from the wall tiles. Similar to the CIII case, the filament in D_α emission follows the local pitch of the magnetic field, and the apparent break in the filament line is due to the absence of recycling at the ϕ=15 deg port. Interestingly, when ELM-driven particles interact with the carbon wall, the relative increase in D_α emission is larger than the increase in CIII emission (both compared to inter-ELM images), possibly suggesting that ELM-wall interactions release deposited deuterium[38] from the wall more

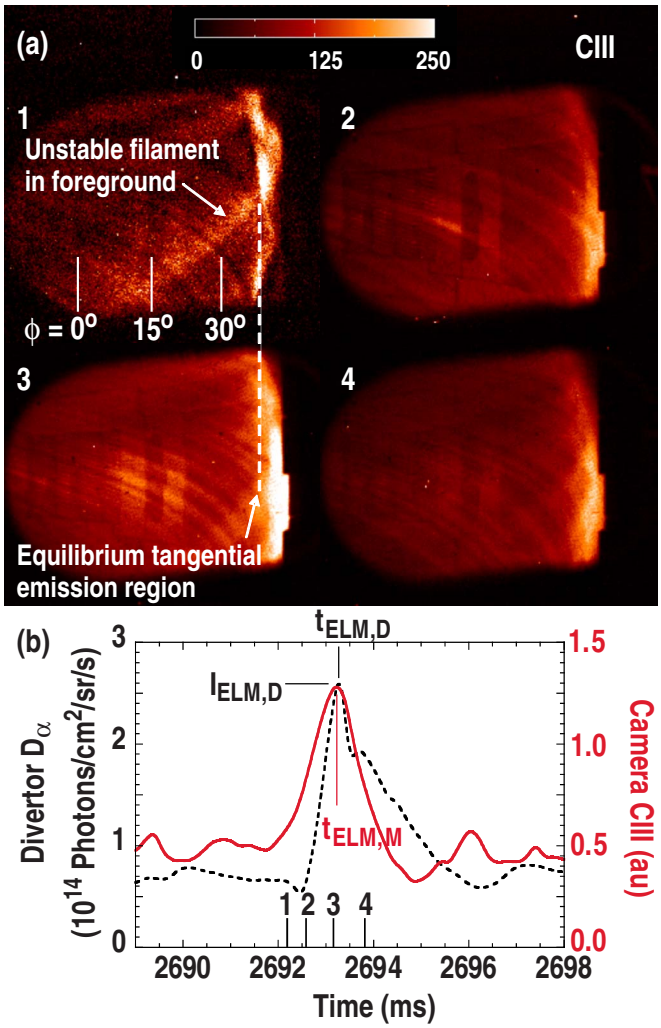

FIG. 2. (Color online) Images in CIII light of an ELM-driven plasma (shot 126529) show multiple field-aligned filaments are ejected into the SOL. The first image in (a) has the background light subtracted and shows an unstable filament wrapping from the foreground of the image around the right side of the plasma edge. (b) The integrated camera intensity is compared to the inner divertor D_α signal, and the times of images 1–4 are labeled.

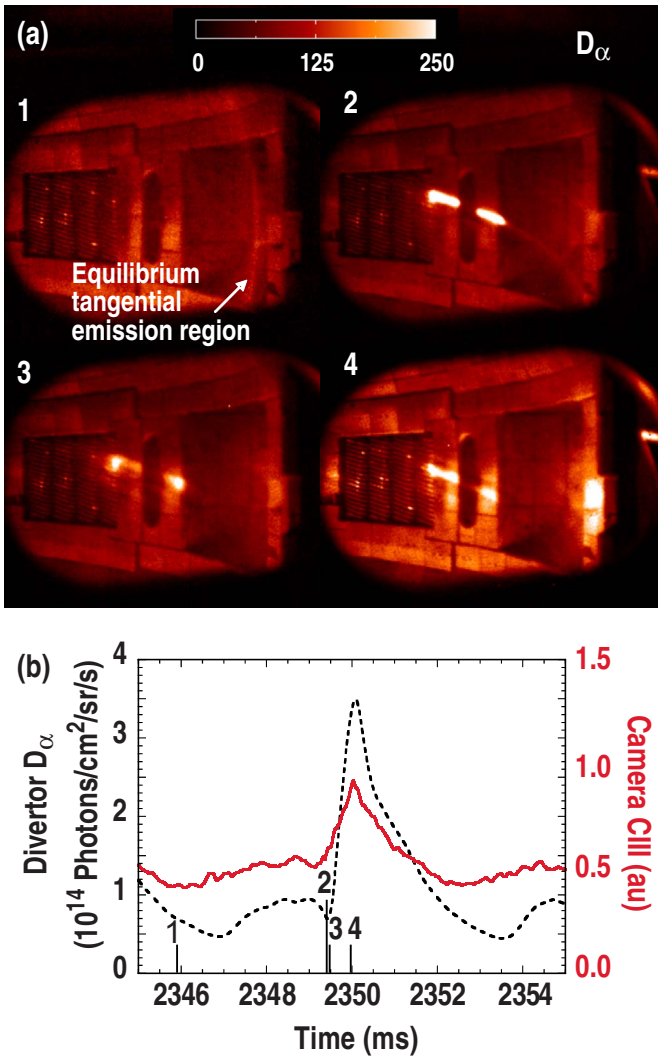

FIG. 3. (Color online) (a) Images in D_α light (shot 126532) show ELM filaments interacting with the wall. The time trace (b) shows D_α light from the midplane region compared to the inner divertor during an ELM.

readily than carbon. Comparing the fourth image to the other three images shows that when particles arrive at the divertor, the emitted D_α light from the divertor is reflected from the midplane wall, which reduces contrast and could affect interpretation of spectroscopic-based diagnostics.

Multiple filament-wall interactions are typically observed in succession during a single ELM event. In Fig. 4, we plot the time series of a one-dimensional (1D) vertical profile of light intensity viewed at the outer wall at $\phi=12$ deg, and the times marked 2, 3, and 4 correspond to the times of the second, third, and fourth images in Fig. 3(a). The profile intensity is adjusted to show interactions with the outer wall. Figure 4 shows that the first filament which hits the wall at $Z=6$ cm at $t=2349.42$ ms is distinct from the bright filament seen ~ 500 μs later at $Z=1$ cm. The image data complement probe data that have previously shown a transient increase in density and temperature as individual filaments transited the probe location in the SOL.[12] Observations of multiple filaments in succession during a single ELM are qualitatively consistent with nonlinear BOUT calculations that show explosive growth of filaments, and possible secondary instabilities driving the radial breakup of radially extended filaments.[39] Alternatively, the appearance of multiple filaments in succession may be due to toroidal (or poloidal) rotation of the filaments and variation in the time of filament ejection.

Based on the camera data, the filaments rotate. However, due to the pitch of the filaments and the limitations of the camera field of view, it is difficult to distinguish between the toroidal and poloidal rotation directions. Previous interpretations of probe data[12] and asymmetries observed in power deposition structures on tile array data[40] are consistent with the paradigm of toroidal rotation of filaments, and for the discussion here we assume the filaments rotate toroidally. The camera-observed filament motion corresponds to rotation in the cocurrent direction in lower single null magnetic configuration with normal B_T and corresponds to rotation in the countercurrent direction in upper single null with reversed B_T. Based on images, the estimated filament toroidal

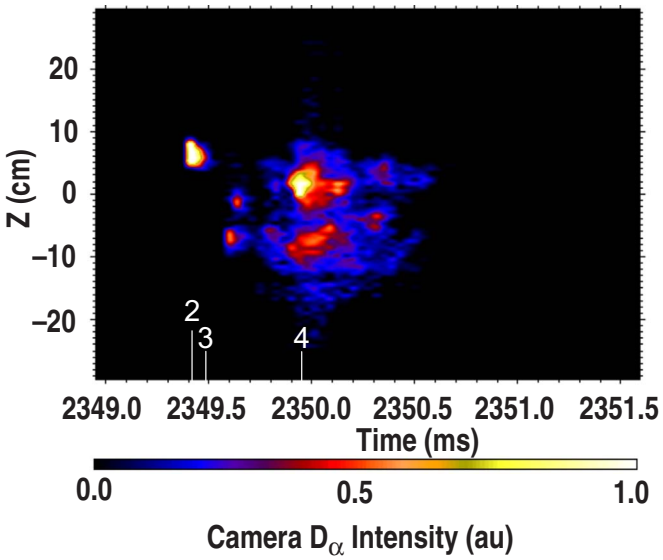

FIG. 4. (Color online) Time trace of 1D vertical profile of D_α emission from the outer wall recorded by the fast camera, showing multiple filaments interact with the wall during a single ELM event. The numbers correspond to the times in Fig. 3.

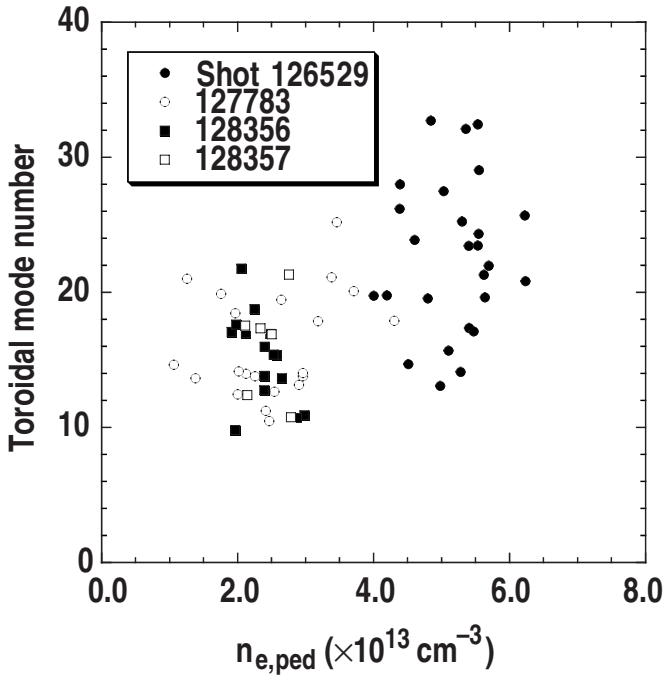

FIG. 5. Measured ELM toroidal mode number n vs pedestal density, showing a general trend of n increasing with density.

velocity ranges from <1 to 10 km/s at a radial location ~ 2 cm outside the separatrix, and ranges from <1 to 4 km/s at the wall. The measured carbon ion toroidal rotation velocity using charge exchange recombination (CER) at the pedestal is approximately 55 km/s and decreases with radius. Estimates of the radial location of the D_α emission seen by the camera correspond to CER-measured toroidal velocities ranging from 10 to 30 km/s, suggesting that the filaments rotate at or slightly below the rotation velocity of carbon ions. An upper bound on the far-SOL toroidal rotation velocity v_ϕ is estimated based on the ability to resolve individual filaments toroidally separated by $\Delta\phi \sim 20$ deg with exposure times as slow as $\tau_{exp}=200$ μs, yielding $v_\phi < R\Delta\phi/\tau_{exp} \sim 5$ km/s for CIII light seen in the mid to far region of the SOL. The numbers presented here may help constrain ELM models that include toroidal rotation.

IV. ELM MODE STRUCTURE

The mode structure of ELMs is measured from the toroidal separation $\Delta\phi$ of adjacent filaments, and Fig. 5 shows the toroidal mode number $n \equiv 2\pi/\Delta\phi$ vs pedestal density $n_{e,ped}$. Light from CIII emission at the onset of the ELM instability is used for the measurements, and due to limitations of the camera toroidal field of view, only $n > 9$ can be measured. The mode number is typically $\sim 20\%$ higher in the late nonlinear phase of the ELM, which is a similar observation to the growth of the inferred mode numbers throughout the ELM evolution in ASDEX Upgrade.[41] We find that ELMs are smaller and have a higher toroidal mode number at high density, consistent with ELITE[37,39] code calculations showing that the most unstable n increases as the edge current density decreases, which is expected at high density due to collisional suppression of the bootstrap current. In the low-density case, strong edge currents may develop with minimal collisional suppression. ELITE code calculations show that edge currents reduce edge magnetic shear and this reduction stabilizes high n ballooning modes, while edge currents drive intermediate to low n peeling modes.

V. PARALLEL SOL FLOW DURING ELMS

At high density, the time delay between the ELM signal measured by the camera at the outer-midplane and the D_α ELM signal from the inner divertor is consistent with the model of parallel convective transport of ions in the SOL; however, at low density the midplane-divertor time delay measurements are still open to interpretation. The time $t_{ELM,M}$ of the peak ELM signal measured by the camera is compared to the time $t_{ELM,D}$ of the peak inner divertor signal; examples of these times are shown in Fig. 2(b). The midplane-divertor delay $\Delta t_{MD} \equiv t_{ELM,D} - t_{ELM,M}$ is calculated and plotted in Fig. 6 versus the peak ELM intensity I_{ELM} measured at the divertor. The CIII camera data marked as solid circles show that in high-density plasmas with normalized electron pedestal collisionality $\nu^*_{ped}=0.50$, particles ejected into the SOL from larger ELMs experience faster parallel transport than that from smaller ELMs, presumably because larger ELMs have broader eigenmodes that eject particles from deeper within the plasma with higher temperature compared to particles ejected by smaller ELMs.[30] This interpretation of the time delay data is supported by previous stability calculations of ELITE showing that the ELM size correlates with the radial depth of the most unstable mode.[36] Ions ejected into the SOL from the low-field-side midplane region undergo parallel transport over the top of the tokamak (in lower single null magnetic configuration), into the high-field-side region of the SOL, and down to the inner divertor target, with a parallel connection length of

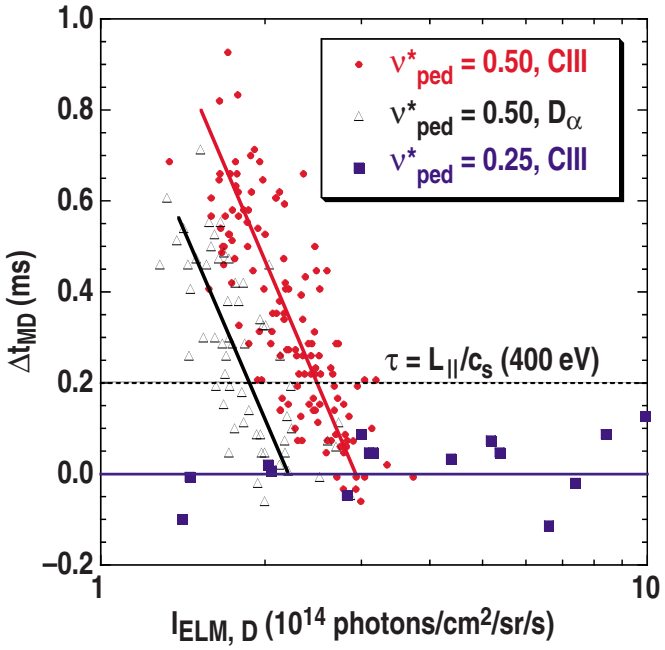

FIG. 6. (Color online) The time delay Δt_{MD} between ELM signals measured at the midplane (camera) and divertor (D_α photodiode) are plotted vs ELM size $I_{ELM,D}$. In moderate collisionality, the time delay is larger for smaller ELMs. The shift between the lines drawn for camera measurements in CIII (circles) and D_α (triangles) shows that the midplane D_α ELM signal appears later than the midplane CIII signal. In lower collisionality plasmas (squares) the midplane and divertor ELM signals appear simultaneously for all ELM sizes.

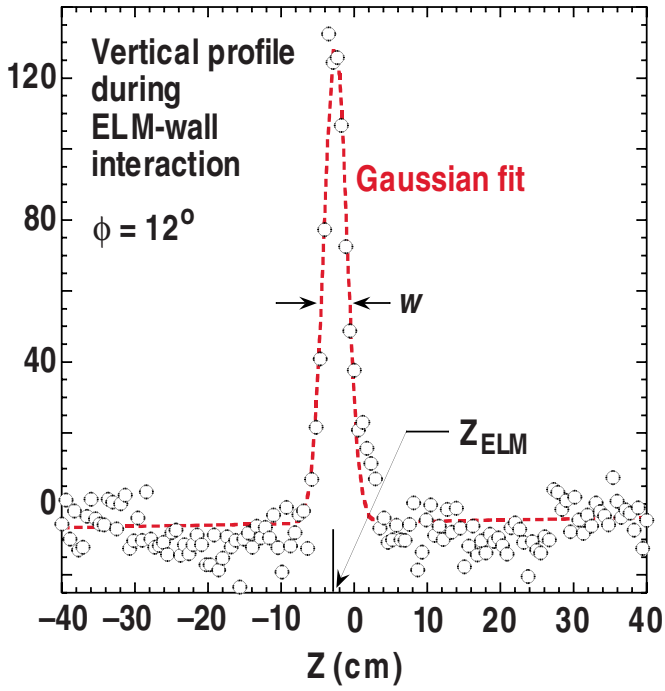

FIG. 7. (Color online) 1D vertical profile of camera signal during an ELM-wall interaction at ϕ=12 deg, with background light subtracted. A Gaussian fit is shown as the dashed line.

$L_{||} \equiv 2\pi R q_{95} \sim 40$ m. The pedestal ion temperature for the high-density case is ~400 eV with the ion sound speed $c_{s,\mathrm{ped}} \sim 200$ km/s; in Fig. 6, the time lag $\tau = L_{||}/c_{s,\mathrm{ped}}$ is shown as a dashed line for reference.

The high-density case with D_α camera data (triangle symbols in Fig. 6) shows the general trend of faster parallel transport for larger ELMs; in addition, the midplane D_α data have a slightly smaller time delay compared to the midplane CIII case (plasma conditions were similar in both cases, and the divertor measurements were in D_α light for all data in Fig. 6). Thus, the midplane D_α signal appears later than the midplane CIII signal by ~300 μs, possibly because the peak ELM intensity of the camera signal in D_α light occurs when filaments interact with the outer wall, while the peak CIII signal may occur in the SOL.

In low-density plasmas with $\nu^*_{\mathrm{ped}} = 0.25$ (square symbols in Fig. 6), the ELM signals appear simultaneously at the midplane and the divertor, showing a qualitatively different behavior compared to the high-density case. The data suggest that in low-density plasmas, a more poloidally symmetric ELM mode structure may exist, or possibly local effects at the inner divertor play a role.[35] Pedestal measurements have previously shown that ELMs cause a larger reduction of pedestal temperature in low-density plasmas ("conductive" ELMs) than in high-density plasmas ("convective" ELMs),[42,43] suggesting that collisional restriction of heat flowing along filaments may be related to the difference in ELM behavior. Another possibility is that in high-density plasmas, collisional suppression of edge currents reduces the peeling nature of the instability and the ELM is driven by a coupled peeling-ballooning instability, while in low-density plasmas, the ELM instability is peeling-dominated. Ballooning filaments would first be ejected into the SOL at the low-field-side midplane while possibly remaining attached near the magnetic X-point. The filaments would then act as conduits for parallel transport of particles and heat that drain from a region within the plasma that depends on the ELM size. A peeling-dominated instability, however, might cause an edge transport barrier collapse that affects the plasma in a more poloidally uniform manner, and thus the midplane and divertor ELM signals would appear simultaneously. Recent simulations support this speculation by showing that the linear peeling mode eigenfunction is more poloidally uniform than the linear ballooning eigenfunction.[44]

VI. ELM-WALL INTERACTIONS

Images of ELM-wall interaction in D_α light are used here to develop the distribution of the poloidal width of filaments and distribution of the location where ELMs hit the outer-midplane wall. The fast camera field of view has a vertical range of $-45 < Z < 45$ cm; thus, the particle and heat flux to surfaces outside this region are not considered here. A vertical 1D profile of the light intensity at ϕ=12 deg is obtained by subtracting a time-averaged background (inter-ELM) image from an image during an ELM-wall interaction, such as that shown in the second image of Fig. 3(a). A Gaussian fit is made to the 1D perturbation profile signal as shown in Fig. 7. The poloidal width w of the filament light at the wall and the vertical location Z_{ELM} of the ELM-wall interaction are then recorded for over 200 events in high-

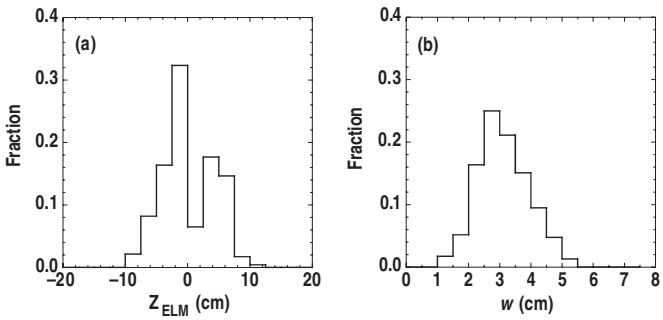

FIG. 8. Distributions of (a) vertical location Z_{ELM} where ELM filaments strike the outer wall, and (b) poloidal filament width w for shots 126531 and 126532.

density discharges with $\nu^*_{ped}=0.5$. Figure 8(a) shows that the distribution of ELM-wall interactions is localized to within ± 15 cm of the midplane, suggesting that sensitive diagnostics could be placed above or below the midplane to avoid possible damage in future devices. A gap between wall tiles at the midplane is responsible for the lack of wall interactions at $Z=0$. The poloidal localization of the initial expulsion is qualitatively consistent with CER data presented in Ref. 43. The measured poloidal (or vertical) width of the filament ranges from 1 to 5 cm, with a mean poloidal width of 3 cm as shown in Fig. 8(b). Assuming tube-like filaments with roughly equal radial and poloidal widths, the camera measurements of the filament widths are roughly consistent with previous probe measurements of individual filaments transiting the probe location in a time of 20–40 μs at a radial velocity of 500 m/s. We note that finite camera exposure times combined with toroidal rotation could spuriously increase the measured widths, and may be responsible for the slight asymmetry seen in the filament width distribution.

VII. CONCLUSIONS

Fast imaging of ELMs in the low-field-side midplane of DIII-D demonstrates that ELMs begin with an unstable filament or group of filaments bulging radially outward into the SOL, and that multiple filaments are then ejected within a few hundred μs in rapid succession. The filaments are aligned with the local magnetic field and rotate toroidally and/or poloidally. Due to cross-field transport, a significant fraction of ELMs interact with the midplane wall and release neutrals, and the filament-wall interactions are localized within ± 15 cm of the midplane. The filament widths range from 1 to 5 cm, consistent with previous probe measurements of filaments transiting the probe location. The measured mode numbers show qualitative agreement with the peeling-ballooning model, which postulates that ELMs are a limit cycle driven by a combination of current and pressure-gradient MHD instabilities.[39,45] The toroidal and poloidal mode numbers of the ELM filamentary structure depend on plasma density, with the measured toroidal mode number ranging from 10 to 20 in low-density plasmas and 15 to 35 in high-density plasmas. Comparing the fast camera midplane data with the inner divertor D_α signal shows that in high-density plasmas, parallel transport velocities depend on the ELM amplitude, suggesting that the ELM size is related to the eigenmode width,[46,47] with larger ELMs corresponding to broader eigenmodes. The larger eigenmode widths result in deeper (and thus hotter) plasma being ejected during the ELM crash, and thus faster parallel transport. The simultaneous ELM signal at the midplane and divertor in low-density plasmas suggests qualitatively different ELM behavior in low-density plasmas versus high density, possibly due to a transition from a coupled peeling-ballooning instability in high density to a more current-driven peeling type of instability in low density.

ACKNOWLEDGMENTS

This work was supported by the U.S. Department of Energy under Contract Nos. DE-FG02-04ER54758 and DE-FG03-95ER54309.

[1] J. W. Connor, Plasma Phys. Controlled Fusion **40**, 531 (1998).
[2] W. Suttrop, Plasma Phys. Controlled Fusion **42**, A1 (2000).
[3] A. W. Leonard, N. Asakura, J. A. Boedo, M. Becoulet, G. F. Counsell, T. Eich, W. Fundamenski, A. Herrmann, L. D. Horton, Y. Kamada, A. Kirk, B. Kurzan, A. Loarte, J. Neuhauser, I. Nunes, N. Oyama, R. A. Pitts, G. Saibene, C. Silva, P. B. Snyder, H. Urano, M. R. Wade, H. R. Wilson, and for the Pedestal and Edge Physics ITPA Topical Group, Plasma Phys. Controlled Fusion **48**, A149 (2006).
[4] F. Wagner, G. Becker, K. Behringer, D. Campbell, A. Eberhagen, W. Engelhardt, G. Fussmann, O. Gehre, J. Gernhardt, G. v. Gierke, G. Haas, M. Huang, F. Karger, M. Keilhacker, O. Klüber, M. Kornherr, K. Lackner, G. Lisitano, G. G. Lister, H. M. Mayer, D. Meisel, E. R. Müller, H. Murmann, H. Niedermeyer, W. Poschenrieder, H. Rapp, H. Röhr, F. Schneider, G. Siller, E. Speth, A. Stäbler, K. H. Steuer, G. Venus, O. Vollmer, and Z. Yü, Phys. Rev. Lett. **49**, 1408 (1982).
[5] G. Federici, P. Andrew, P. Barabaschi, J. Brooks, R. Doerner, A. Geier, A. Herrmann, G. Janeschitz, K. Krieger, A. Kukushkin, A. Loarte, R. Neu, G. Saibene, M. Shimada, G. Strohmayer, and M. Sugihara, J. Nucl. Mater. **313–316**, 11 (2003).
[6] A. W. Leonard, T. H. Osborne, M. E. Fenstermacher, C. J. Lasnier, and M. A. Mahdavi, J. Nucl. Mater. **290–293**, 1097 (2001).
[7] S. Morita, T. Morisaki, M. Goto, K. Tanaka, M. B. Chowdhuri, K. Ikeda, R. Katai, S. Masuzaki, K. Nagaoka, K. Narihara, Y. Oka, M. Osakabe, S. Sakakibara, Y. Takeiri, K. Tsumori, H. Yamazaki, K. Y. Watanabe, and LHD Experimental Group, Nucl. Fusion **47**, 1033 (2007).
[8] A. Weller, M. Anton, J. Geiger, M. Hirsch, R. Jaenicke, A. Werner, C. Nührenberg, E. Sallander, and D. A. Spong, Phys. Plasmas **8**, 931 (2001).
[9] I. García-Cortés, E. de la Luna, F. Castejón, J. A. Jiménez, E. Ascasíbar, B. Brañas, T. Estrada, J. Herranz, A. López-Fraguas, I. Pastor, J. Qin, J. Sánchez, F. L. Tabarés, D. Tafalla, V. Tribaldos, B. Zurro, TJ-II Team, and S. V. Shchepetov, Nucl. Fusion **40**, 1867 (2000).
[10] P. Gohil, M. A. Mahdavi, L. Lao, K. H. Burrell, M. S. Chu, J. C. DeBoo, C. L. Hsieh, N. Ohyabu, R. T. Snider, R. D. Stambaugh, and R. E. Stockdale, Phys. Rev. Lett. **61**, 1603 (1988).
[11] M. E. Fenstermacher, T. H. Osborne, A. W. Leonard, P. B. Snyder, D. M. Thomas, J. A. Boedo, T. A. Casper, R. J. Groebner, M. Groth, M. A. H. Kempenaars, A. Loarte, G. R. McKee, W. M. Meyer, G. Saibene, M. A. VanZeeland, X. Q. Xu, L. Zeng, and the DIII-D Team, Nucl. Fusion **45**, 1493 (2005).
[12] J. A. Boedo, D. L. Rudakov, E. Hollmann, D. S. Gray, K. H. Burrell, R. A. Moyer, G. R. McKee, R. Fonck, P. C. Stangeby, T. E. Evans, P. B. Snyder, A. W. Leonard, M. A. Mahdavi, M. J. Schaffer, W. P. West, M. E. Fenstermacher, M. Groth, S. L. Allen, C. Lasnier, G. D. Porter, N. S. Wolf, R. J. Colchin, L. Zeng, G. Wang, J. G. Watkins, and T. Takahashi, Phys. Plasmas **12**, 072516 (2005).
[13] M. R. Wade, K. H. Burrell, A. W. Leonard, T. H. Osborne, and P. B. Snyder, Phys. Rev. Lett. **94**, 225001 (2005).
[14] A. Sykes, R. J. Akers, L. C. Appel, E. R. Arends, P. G. Carolan, N. J. Conway, G. F. Counsell, G. Cunningham, A. Dnestrovskij, Yu. N. Dnestrovskij, A. R. Field, S. J. Fielding, M. P. Gryaznevich, S. Korsholm, E. Laird, R. Martin, M. P. S. Nightingale, C. M. Roach, M. R. Tournianski,

M. J. Walsh, C. D. Warrick, H. R. Wilson, S. You, MAST Team, and NBI Team, Nucl. Fusion **41**, 1423 (2001).
[15]A. Kirk, H. R. Wilson, G. F. Counsell, R. Akers, E. Arends, S. C. Cowley, J. Dowling, B. Lloyd, M. Price, and M. Walsh, Phys. Rev. Lett. **92**, 245002 (2004).
[16]A. Herrmann and O. Gruber, Fusion Sci. Technol. **44**, 569 (2003).
[17]I. Nunes, G. D. Conway, A. Loarte, M. Manso, F. Serra, W. Suttrop, and the CFN and ASDEX Upgrade teams, Nucl. Fusion **44**, 883 (2004).
[18]I. H. Hutchinson, R. Boivin, F. Bombarda, P. Bonoli, S. Fairfax, C. Fiore, J. Goetz, S. Golovato, R. Granetz, M. Greenwald, S. Horne, A. Hubbard, J. Irby, B. LaBombard, B. Lipschultz, E. Marmar, G. McCracken, M. Porkolab, J. Rice, J. Snipes, Y. Takase, J. Terry, S. Wolfe, C. Christensen, D. Garnier, M. Graf, T. Hsu, T. Luke, M. May, A. Niemczewski, G. Tinios, J. Schachter, and J. Urbahn, Phys. Plasmas **1**, 1511 (1994).
[19]D. A. Mossessian, P. B. Snyder, A. Hubbard, J. W. Hughes, M. Greenwald, B. LaBombard, J. A. Snipes, S. Wolfe, and H. Wilson, Phys. Plasmas **10**, 1720 (2003).
[20]P. H. Rebut, R. J. Bickerton, and B. E. Keen, Nucl. Fusion **25**, 1011 (1985).
[21]Ph. Ghendrih, Y. Sarazin, M. Bécoulet, G. Huysmans, S. Benkadda, P. Beyer, C. Figarella, X. Garbet, and P. Monier-Garbet, J. Nucl. Mater. **313–316**, 914 (2003).
[22]M. Ono, M. G. Bell, R. E. Bell, T. Bigelow, M. Bitter, W. Blanchard, J. Boedo, C. Bourdelle, C. Bush, W. Choe, J. Chrzanowski, D. S. Darrow, S. J. Diem, R. Doerner, P. C. Efthimion, J. R. Ferron, R. J. Fonck, E. D. Fredrickson, G. D. Garstka, D. A. Gates, T. Gray, L. R. Grisham, W. Heidbrink, K. W. Hill, D. Hoffmann, T. R. Jarboe, D. W. Johnson, R. Kaita, S. M. Kaye, C. Kessel, J. H. Kim, M. W. Kissick, S. Kubota, H. W. Kugel, B. P. LeBlanc, K. Lee, S. G. Lee, B. T. Lewicki, S. Luckhardt, R. Maingi, R. Majeski, J. Manickam, R. Maqueda, T. K. Mau, E. Mazzucato, S. S. Medley, J. Menard, D. Mueller, B. A. Nelson, C. Neumeyer, N. Nishino, C. N. Ostrander, D. Pacella, F. Paoletti, H. K. Park, W. Park, S. F. Paul, Y.-K. M. Peng, C. K. Phillips, R. Pinsker, P. H. Probert, S. Ramakrishnan, R. Raman, M. Redi, A. L. Roquemore, A. Rosenberg, P. M. Ryan, S. A. Sabbagh, M. Schaffer, R. J. Schooff, R. Seraydarian, C. H. Skinner, A. C. Sontag, V. Soukhanovskii, J. Spaleta, T. Stevenson, D. Stutman, D. W. Swain, E. Synakowski, Y. Takase, X. Tang, G. Taylor, J. Timberlake, K. L. Tritz, E. A. Unterberg, A. Von Halle, J. Wilgen, M. Williams, J. R. Wilson, X. Xu, S. J. Zweben, R. Akers, R. E. Barry, P. Beiersdorfer, J. M. Bialek, B. Blagojevic, P. T. Bonoli, M. D. Carter, W. Davis, B. Deng, L. Dudek, J. Egedal, R. Ellis, M. Finkenthal, J. Foley, E. Fredd, A. Glasser, T. Gibney, M. Gilmore, R. J. Goldston, R. E. Hatcher, R. J. Hawryluk, W. Houlberg, R. Harvey, S. C. Jardin, J. C. Hosea, H. Ji, M. Kalish, J. Lowrance, L. L. Lao, F. M. Levinton, N. C. Luhmann, R. Marsala, D. Mastravito, M. M. Menon, O. Mitarai, M. Nagata, G. Oliaro, R. Parsells, T. Peebles, B. Peneflor, D. Piglowski, G. D. Porter, A. K. Ram, M. Rensink, G. Rewoldt, J. Robinson, P. Roney, K. Shaing, S. Shiraiwa, P. Sichta, D. Stotler, B. C. Stratton, R. Vero, W. R. Wampler, and G. A. Wurden, Plasma Phys. Controlled Fusion **45**, A335 (2003).
[23]R. Maingi, C. E. Bush, E. D. Fredrickson, D. A. Gates, S. M. Kaye, B. P. LeBlanc, J. E. Menard, H. Meyer, D. Mueller, N. Nishino, A. L. Roquemore, S. A. Sabbagh, K. Tritz, S. J. Zweben, M. G. Bell, R. E. Bell, T. Biewer, J. A. Boedo, D. W. Johnson, R. Kaita, H. W. Kugel, R. J. Maqueda, T. Munsat, R. Raman, V. A. Soukhanovskii, T. Stevenson, and D. Stutman, Nucl. Fusion **45**, 1066 (2005).
[24]A. Kitsunezaki, M. Shimizu, H. Ninomiya, M. Kutiyama, and the JT-60 Team, Fusion Sci. Technol. **42**, 179 (2002).
[25]N. Oyama, N. Asakura, A. V. Chankin, T. Oikawa, M. Sugihara, H. Takenaga, K. Itami, Y. Miura, Y. Kamada, K. Shinohara, and the JT-60 Team, Nucl. Fusion **44**, 582 (2004).
[26]A. Kirk, B. Koch, R. Scanell, H. R. Wilson, G. Counsell, J. Dowling, A. Herrmann, R. Martin, and M. Walsh, Phys. Rev. Lett. **96**, 185001 (2006).
[27]A. Kirk, T. Eich, A. Herrmann, H. W. Muller, L. D. Horton, G. F. Counsell, M. Price, V. Rohde, V. Bobkov, B. Kurzan, J. Neuhauser, H. Wilson, and the ASDEX Upgrade and MAST Teams, Plasma Phys. Controlled Fusion **47**, 995 (2005).
[28]A. Kirk, N. Ben Ayed, G. Counsell, B. Dudson, T. Eich, A. Herrmann, B. Koch, R. Martin, A. Meakins, S. Saarelma, R. Scannell, S. Tallents, M. Walsh, H. R. Wilson, and the MAST team, Plasma Phys. Controlled Fusion **48**, B433 (2005).
[29]T. Eich, A. Herrmann, and J. Neuhauser, Phys. Rev. Lett. **91**, 195003 (2003).
[30]T. H. Osborne, J. R. Ferron, R. J. Groebner, L. L. Lao, A. W. Leonard, M. A. Mahdavi, P. B. Snyder, and the DIII-D Team, *Proceedings of the 29th EPS Conference on Plasma Physics and Controlled Fusion, Montreux, Switzerland*, ECA Vol. 26B (European Physical Society, Paris, 2002), p. 1.062.
[31]D. L. Rudakov, J. A. Boedo, R. A. Moyer, P. C. Stangeby, J. G. Watkins, D. G. Whyte, L. Zeng, N. H. Brooks, R. P. Doerner, T. E. Evans, M. E. Fenstermacher, M. Groth, E. M. Hollmann, S. I. Krasheninnikov, C. J. Lasnier, A. W. Leonard, M. A. Mahdavi, G. R. McKee, A. G. McLean, A. Yu. Pigarov, W. R. Wampler, G. Wang, W. P. West, and C. P. C. Wong, Nucl. Fusion **45**, 1589 (2005).
[32]W. P. West, N. H. Brooks, M. E. Fenstermacher, R. C. Isler, G. L. Jackson, C. J. Lasnier, A. Ramsey, M. R. Wade, D. G. Whyte, and R. D. Wood, J. Nucl. Mater. **266–269**, 732 (1999).
[33]J. R. Ferron, M. L. Walker, L. L. Lao, H. E. St. John, D. A. Humphreys, and J. A. Leuer, Nucl. Fusion **38**, 1055 (1998).
[34]M. E. Fenstermacher, S. L. Allen, N. H. Brooks, D. A. Buchenauer, T. N. Carlstrom, J. W. Cuthbertson, E. J. Doyle, T. E. Evans, P.-M. Garbet, R. W. Harvey, D. N. Hill, A. W. Hyatt, R. C. Isler, G. Jackson, R. A. James, R. Jong, C. C. Klepper, C. J. Lasnier, A. W. Leonard, M. A. Mahdavi, R. Maingi, W. H. Meyer, R. A. Moyer, D. G. Nilson, T. W. Petrie, G. D. Porter, T. L. Rhodes, M. J. Schaffer, R. D. Stambaugh, D. M. Thomas, S. Tugarinov, M. R. Wade, J. G. Watkins, W. P. West, D. G. Whyte, and R. D. Wood, Phys. Plasmas **4**, 1761 (1997).
[35]M. E. Fenstermacher, A. W. Leonard, P. B. Snyder, J. A. Boedo, N. H. Brooks, R. J. Colchin, D. S. Gray, R. J. Groebner, M. Groth, E. Hollmann, C. J. Lasnier, T. H. Osborne, T. W. Petrie, D. L. Rudakov, H. Takahashi, J. G. Watkins, L. Zeng, and the DIII-D Team, Plasma Phys. Controlled Fusion **45**, 1597 (2003).
[36]P. B. Snyder, J. R. Wilson, J. R. Ferron, L. L. Lao, A. W. Leonard, T. H. Osborne, A. D. Turnbull, D. Mossessian, M. Murakami, and X. Q. Xu, Phys. Plasmas **9**, 2037 (2002).
[37]H. R. Wilson, P. B. Snyder, G. T. A. Huysmans, and R. L. Miller, Phys. Plasmas **9**, 1277 (2002).
[38]J. Roth, A. Kirschner, W. Bohmeyer, S. Brezinsek, A. Cambe, E. Casarotto, R. Doerner, E. Gauthier, G. Federici, S. Higashijima, J. Hogan, A. Kallenbach, H. Kubo, J. M. Layet, T. Nakano, V. Philipps, A. Pospieszczyk, R. Preuss, R. Pugno, R. Ruggiéri, B. Schweer, G. Sergienko, and M. Stamp, J. Nucl. Mater. **337–339**, 970 (2005).
[39]P. B. Snyder, H. R. Wilson, and X. Q. Xu, Phys. Plasmas **12**, 056115 (2005).
[40]T. E. Evans, C. J. Lasnier, D. N. Hill, A. W. Leonard, M. E. Fenstermacher, T. W. Petrie, and M. J. Schaffer, J. Nucl. Mater. **220–222**, 235 (1995).
[41]T. Eich, A. Herrmann, J. Neuhauser, R. Dux, J. C. Fuchs, S. Günter, L. D. Horton, A. Kallenbach, P. T. Lang, C. F. Maggi, M. Maraschek, V. Rohde, W. Schneider, and the ASDEX Upgrade Team, Plasma Phys. Controlled Fusion **47**, 815 (2005).
[42]A. W. Leonard, T. H. Osborne, M. E. Fenstermacher, R. J. Groebner, M. Groth, C. J. Lasnier, M. A. Mahdavi, T. W. Petrie, P. B. Snyder, J. G. Watkins, and L. Zeng, Phys. Plasmas **10**, 1765 (2003).
[43]M. R. Wade, K. H. Burrell, J. T. Hogan, A. W. Leonard, T. H. Osborne, P. B. Snyder, and D. Coster, Phys. Plasmas **12**, 056120 (2005).
[44]N. Mizuguchi, R. Khan, T. Hayashi, and N. Nakajima, Nucl. Fusion **47**, 579 (2007).
[45]H. R. Wilson, S. C. Cowley, A. Kirk, and P. B. Snyder, Plasma Phys. Controlled Fusion **48**, A71 (2006).
[46]J. R. Ferron, M. S. Chu, G. L. Jackson, L. L. Lao, R. L. Miller, T. H. Osborne, P. B. Snyder, E. J. Strait, T. S. Taylor, A. D. Turnbull, A. M. Garofalo, M. A. Makowski, B. W. Rice, M. S. Chance, L. R. Baylor, M. Murakami, and M. R. Wade, Phys. Plasmas **7**, 1976 (2000).
[47]L. L. Lao, Y. Kamada, T. Oikawa, L. R. Baylor, K. H. Burrell, V. S. Chan, M. S. Chance, M. S. Chu, J. R. Ferron, T. Fukuda, T. Hatae, A. Isayama, G. J. Jackson, A. W. Leonard, M. A. Makowski, J. Manickam, M. Murakami, M. Okabayashi, T. H. Osborne, P. B. Snyder, E. J. Strait, S. Takeji, T. Takizuka, T. S. Taylor, A. D. Turnbull, K. Tsuchiya, and M. R. Wade, Nucl. Fusion **41**, 295 (2001).